mater.scichina.com link.springer.com

Published online 3 July 2020 | https://doi.org/10.1007/s40843-020-1358-5
Sci China Mater 2021, 64(1): 198–208

All-inorganic $Cs_2AgBiBr_6$/CuSCN-based photodetectors for weak light imaging

Genghua Yan[1], Zhong Ji[1], Zhuowei Li[1], Bangqi Jiang[1], Min Kuang[3], Xiang Cai[4], Ye Yuan[1*] and Wenjie Mai[1,2*]

ABSTRACT **Weak light imaging has drawn more and more attention because of its promising potential for practical applications in security monitoring and space exploration. In this work, all-inorganic $Cs_2AgBiBr_6$ double perovskite-based self-powered photodetectors containing inorganic copper thiocyanate (CuSCN) as hole-transport layers (HTLs) are successfully fabricated and applied for weak light imaging, which is the first report on the weak light imaging application of all-inorganic lead-free perovskite photodetectors. CuSCN films with favorable optical property and hole extraction capability are prepared *via* a cost efficient and fast solvent removal method, demonstrating the potential for high-performance perovskite-based devices as transparent components. It is revealed that the band alignment of the device is effectively optimized with the presence of CuSCN HTLs, which can availably transport holes while block electrons at the $Cs_2AgBiBr_6$/CuSCN interface, resulting in remarkable improvement of photoresponse performance. The responsivity and detectivity are 0.34 A W^{-1} and 1.03×10^{13} Jones, respectively. In particular, the light current has a boost of almost 10 times. Furthermore, the photodetectors are integrated into a self-built light detection imaging system utilizing the focused laser scanning imaging mode. With illumination of as low as 5 nW cm^{-2} (405 nm), the image involving graphics and words with a size of 5 cm×5 cm can still be distinctly recognized. These results suggest the promising potential of all-inorganic perovskite-based devices for weak light detection and imaging applications.**

Keywords: photodetector, weak light imaging, all-inorganic perovskite, $Cs_2AgBiBr_6$ double perovskite, CuSCN inorganic hole-transport layer

INTRODUCTION

The application of weak light imaging has become a growing interest in the fields of military and civilian, including nighttime monitoring, astronomical photography and biomedical imaging. For instance, imaging problem with extremely low illumination such as in caves can be solved by a high-performance weak light detection imaging system. As the key component of the detection imaging system, the capability of the photodetector (PD) highly determines the post-image reconstruction. For high-quality self-powered photodiode PDs, it is expectantly required to possess high detectivity (D^*), low operating voltage, excellent temperature stability and etc. [1–3]. Nowadays, Si-based and InGaAs-based PDs are the major devices for weak light detection [4,5]. However, the manufacturing costs of these devices, especially the production equipment costs (e.g., plasma-enhanced-chemical-vapor-desposition (PECVD) and molecular-beam-epitaxy (MBE)), are relatively high, limiting the development of large-scale production and the popularity of applications.

Driven by the increasing diversified application scenarios and the requirement of cost efficiency, low-cost high-quality PDs with additional functionality are attracting widespread attention in the field of photoelectric detection. Perovskite materials, one of the most glaring advanced materials in the last decade, have great prospect in the field of photoelectric devices because of the large carrier mobility and high light absorption coefficient [6,7]. Up to now, perovskite materials have been successfully applied for solar cells [8,9], light emitting diodes [10,11] and PDs [2,12]. At present, the most common

[1] Siyuan Laboratory, Guangdong Provincial Engineering Technology Research Center of Vacuum Coating Technologies and New Energy Materials, Department of Physics, Jinan University, Guangzhou 510632, China
[2] Guangdong Provincial Key Laboratory of Optical Fiber Sensing and Communications, Jinan University, Guangzhou 510632, China
[3] Guangdong Institute of New Materials, Guangdong Academy of Sciences, Guangzhou 510650, China
[4] Department of Light Chemical Engineering, Guangdong Polytechnic, Foshan 528041, China
* Corresponding authors (emails: yuanye0602@foxmail.com (Yuan Y); wenjiemai@email.jnu.edu.cn (Mai W))

perovskite materials are the organic-inorganic hybrid perovskite species, which are leady compounds. Sargent's group [13] prepared $MAPbBr_3$-based ($MA=CH_3NH_3^+$) single-crystalline PDs and gained a large responsivity exceeding 4000 A W^{-1} and a wide bandwidth of ~10^8 Hz. Tan *et al.* [14] synthesized two-dimensional (2D) $(C_4H_9NH_3)_2PbBr_4$ crystals and fabricated the corresponding PDs, achieving an extremely low dark current of ~10^{-10} A and an ultrahigh responsivity up to 2100 A W^{-1}. Nevertheless, the proverbial toxicity of lead is a non-negligible issue for actual applications. In addition, the stability issue also requires attention and needs to be addressed. Recently, research on lead-free inorganic perovskite materials has drawn broad concerns, and many relative materials have been explored and applied [15–17]. Among them, the species of inorganic double perovskite materials, such as $Cs_2AgBiBr_6$, $Cs_2AgInCl_6$ and Cs_2SnI_6, are among the most promising candidates owing to their environmentally friendly nature, competent photoelectric capabilities and satisfying stability [18–20]. Tang's group [18] fabricated $Cs_2AgInCl_6$ single crystals-based ultraviolet (UV) PDs with high D^* of 9.60×10^{11} cm $Hz^{1/2}$ W^{-1} (Jones) and low dark current of ~10 pA at 5 V bias. Lei *et al.* [19] fabricated and characterized $Cs_2AgBiBr_6$-based photoconductive detectors, reaching a specific D^* of 5.66×10^{11} Jones and demonstrating a remarkable stability after storage for two weeks.

For perovskite-based devices, the structure of planar heterojunction (PHJ) is cost efficient and more compatible since it can be fully solution-processed at low temperature [21]. In general, the device with a PHJ structure consists of an electron-transporting layer (ETL) and a hole-transporting layer (HTL) for efficient charge extraction. For ETLs, TiO_2 layer is the most frequently used n-type semiconductor and has found mature methods for high-efficiency devices. As for specific demands, ZnO and SnO_2 thin films have been applied as ETLs on perovskite-based optoelectronic devices as well [22–24]. However, with regard to HTLs, some challenges still remain. Organic Spiro-OMeTAD (Spiro-OMeTAD: 2,2′,7,7′-tetrakis (*N*,*N*-di-*p*-methoxyphenyl-amine)9,9′-spiro-bifluorene) and polymer-based poly(triarylamine) (PTAA) thin films are the major HTL materials for high-efficiency devices due to their favorable electrical properties and band matching characteristics [25,26]. Whereas, the costs of these materials are relatively exorbitant for commercial-scale productions. What's more, it is appreciable that the organic ingredients of the above materials are an essential factor affecting the long-term operation and thermal stability of the devices [27]. Hence, developing inexpensive inorganic HTL materials is a promising strategy to settle down the cost and instability issues. Benefiting from the intrinsic p-type semiconductor nature and the satisfying properties of adequate energy levels, high hole mobility and good thermal stability, inorganic copper thiocyanate (CuSCN) has attracted widespread attention for applying on perovskite-based devices [27–29]. In addition, the wide band-gap (E_g=3.6 eV) characteristic of CuSCN ensures the desirable transmittance in the range of visible to near-infrared region, which brings it the attraction for tandem, bifacial or other applications. Jen and coworkers [21] prepared CuSCN *via* a low-temperature solution process and utilized it for $CH_3NH_3PbI_3$ solar cells. Encouragingly, a semitransparent PHJ perovskite solar cell with a power conversion efficiency (PCE) of 10% and an average visible transmittance (AVT) of 25% were achieved. In 2017, Grätzel's group [27] used CuSCN thin films as HTLs for $CsFAMAPbI_{3-x}Br_x$ ($FA=CH(NH_2)_2^+$) perovskite solar cells and obtained a PCE exceeding 20%, rendering it the most promising potential HTL materials for large-scale manufacture. Since then, researches on the further property optimization and expanded application of CuSCN HTLs have received extensive concerns. Nonetheless, as far as we know, all-inorganic photoelectric devices that combine lead-free double perovskite materials with CuSCN HTLs have not been reported yet.

Herein, we fabricate all-inorganic PHJ PDs with the structure of $TiO_2/Cs_2AgBiBr_6$/CuSCN for the first time and demonstrate the application for weak light imaging. The as-prepared PDs are a kind of photodiode. With the addition of CuSCN HTLs, the photoresponse performance is remarkably improved. Both light current and on-off ratio increase by almost an order of magnitude. In addition, benefiting from the favorable transmittance of CuSCN layer, the AVT of the device reaches 62.82%, demonstrating the potential for semi-transparent devices. Furthermore, it is revealed that the CuSCN HTL can transport holes efficiently while block electrons at the $Cs_2AgBiBr_6$/CuSCN interface, resulting from the optimized band alignment. Moreover, the $Cs_2AgBiBr_6$-based PDs are used as an imaging sensor in a self-built focused laser scanning imaging system for weak light imaging for the first time. With illumination of as low as 5 nW cm^{-2} (405 nm), both graphics and words in the image with a size of 5 cm×5 cm can still be clearly identified. These results suggest the great potential of $TiO_2/Cs_2AgBiBr_6$/CuSCN-based all-organic PHJ for photoelectric applications.

EXPERIMENTAL SECTION

Preparation of CuSCN HTLs

The CuSCN films were deposited *via* a spin-coating process along with a fast solvent removal method [27]. Firstly, CuSCN precursor solution was prepared by dissolving 60 mg CuSCN powders (Kanto Chemical Co., Inc., 99.5% purity) into 1 mL diethyl sulfide (Macklin, ≥98% purity) after stirring for half an hour at room temperature. For the spin-coating process, the spin-coating rate was varied from 2000 to 8000 r min^{-1} while the time was fixed at 50 s. When the rate was stable, 50 μL CuSCN precursor solution was quickly added and completed within 1 s. Finally, the samples were annealed at 100°C for 5 min.

Preparation of the $Cs_2AgBiBr_6$-based PDs

F-doped SnO_2 (FTO) glasses (Nippon Sheet Glass Co., Ltd.) were used as the substrates, which were ultrasonically cleaned with deionized water, isopropyl alcohol and ethyl alcohol for 15 min, respectively. TiO_2 ETLs, $Cs_2AgBiBr_6$ double perovskite films and CuSCN HTLs were deposited onto the FTO substrates in sequence. For ETLs, TiO_2 films were prepared *via* an atomic layer deposition (ALD) process. During the process, titanium tetrachloride ($TiCl_4$), H_2O vapor and high-purity N_2 were respectively used as the precursor, reactant and carrier gas while the temperature was fixed at 105°C. The thickness of the TiO_2 ETLs was controlled to be 20 nm. $Cs_2AgBiBr_6$ films were prepared by a one-step spin-coating process. For the $Cs_2AgBiBr_6$ precursor solution, 212.8 mg CsBr powders (Alfa Aesar, 99.999% purity), 93.9 mg AgBr powders (Alfa Aesar, 99.9% purity) and 224.4 mg $BiBr_3$ powders (Alfa Aesar, 99% purity) were dissolved in 1 mL dimethylsulfoxide (DMSO) (MP Biomedicals, 99.9% purity) at 80°C with a concentration of 0.5 mol L^{-1}. After being stirred for 4 h, all of the powders were completely dissolved. Prior to spin-coating, the TiO_2-coated substrates and the solution were pre-heated to 80°C for 5–10 min. After that, the heated precursor solution was spin-coated onto the substrates at 500 r min^{-1} for 6 s and then at 3000 r min^{-1} for 50 s. Then the prepared samples were immediately annealed at 285°C for 5 min. For the CuSCN HTLs, the preparation followed the procedures mentioned above. The whole processes of the $Cs_2AgBiBr_6$ film and CuSCN HTL preparations were performed in an Ar-filled glove box. Finally, Au electrodes were deposited by electron beam evaporation with a thickness of 80 nm through a shadow mask.

Characterization

The surface morphology of the films was characterized by scanning electron microscopy (SEM, FEI NNS450). The composition of the CuSCN films was examined by X-ray photoelectron spectroscopy (XPS, K-ALPHA+) with mono Al Kα radiation. The transmittance was characterized by UV-Vis spectrophotometer (Shimadzu, UV-2600). X-ray diffraction (XRD, Rigaku9000 D8) was used to identify the crystal structure with Cu Kα1 radiation (λ= 1.54056 Å) from 10° to 60° while the photoluminescence (PL) spectra were obtained from a photoluminescence spectroscopy (EI FLS980) with 351 nm laser. For device performance, a self-built measurement system combining a Keithley 2400 source meter, a laser diode (405 nm), an oscilloscope and a pulse generator was used to investigate the photoresponse performance. The spectral response characteristic was measured by a QE-R system (SR830). The response speed was evaluated by combining a pulse laser controlled by a waveform generator and a digital oscilloscope (Tektronix TDS 2012C, 200 MHz). For weak light imaging, a focused laser scanning imaging system consisting of a laser (405 nm), a scanning platform, a driver, a Keithley 2400 source meter and some other optical components was used. In addition, a computer was also applied to control the driver and to process the data through specific algorithm.

RESULTS AND DISCUSSION

Fig. 1a shows the architecture of the $Cs_2AgBiBr_6$-based PDs, which are a conventional regular PHJ of perovskite-based devices. To take advantage of the favorable optical properties of the CuSCN films, the transmittance of the films was optimized by adjusting the spin-coating rate. It is worth mentioning that the CuSCN films were prepared by a fast solvent removal method in order to avoid solvent problem as well as ensure the quality of the $Cs_2AgBiBr_6$ perovskite films. As shown in Fig. S1, the average transmittances in the range of 320–500 nm and in visible region (380–780 nm) increase with the spin-coating rates due to the thinner thickness. Nevertheless, too thin coating films could be adverse to the device performance. Fig. S2 exhibits the light current (I_{light}) and dark current (I_{dark}) of the PDs with the CuSCN layers prepared under different spin-coating rates ranging from 2000 to 8000 r min^{-1}. It is found that the I_{light} presents a trend of increasing first and then decreasing, reaching the maximum value at 7000 r min^{-1}. Regardless of the transmittance, the corrosion time of CuSCN solution on the perovskite film is a considerable factor [27]. It is known that perovskite thin film materials are sensitive to solu-

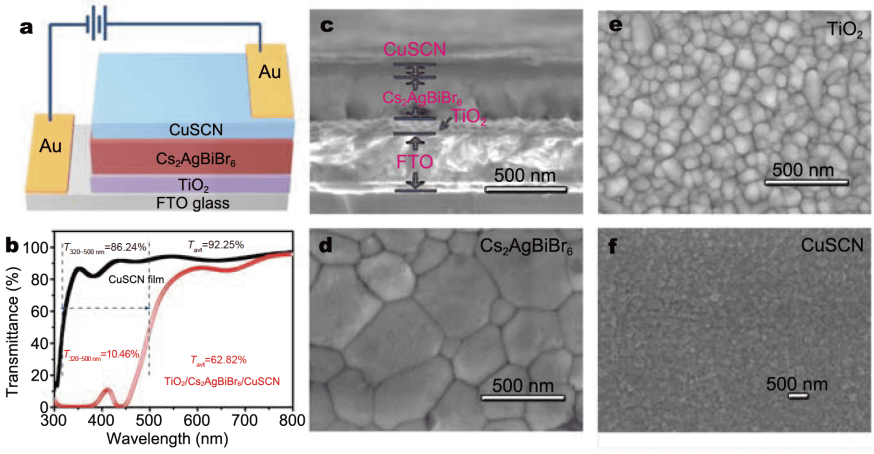

Figure 1 Structural, morphology and optical characterization. (a) Schematic of the $Cs_2AgBiBr_6$-based PD. (b) Transmittance spectra of CuSCN film and the device. (c) Cross-sectional view of the device. Surface morphologies of (d) $Cs_2AgBiBr_6$ film, (e) TiO_2 layer, and (f) CuSCN layer.

tions. They may be dissolved by the solutions, resulting in defects on the surface or in bulk. Therefore, to ensure the quality of the underlying $Cs_2AgBiBr_6$ films, their contact times with CuSCN solution should be as short as possible. Obviously, speeding up the spin-coating rate is beneficial to shortening the corrosion time as well as improving the device performance. Meanwhile, the I_{dark} has little significant changes. Therefore, the spin-coating rate of the CuSCN film was optimized and fixed at 7000 r min^{-1} in the following discussion. Fig. 1b displays the transmittance comparison of the CuSCN film and TiO_2/$Cs_2AgBiBr_6$/CuSCN heterojunction. It is evident that the transmittance difference of the two samples is mainly concentrated in the range of 320–500 nm which is attributed to the absorption of $Cs_2AgBiBr_6$ films. The corresponding absorption spectra of TiO_2, $Cs_2AgBiBr_6$ and CuSCN films are presented in Fig. S3. Besides, it is worth noting that the AVT of TiO_2/$Cs_2AgBiBr_6$/CuSCN heterojunction reaches 62.82%, demonstrating the great potential for serving as semi-transmittance devices. In addition, the transmittance spectrum of the whole PD is shown in Fig. S4, indicating the nice transparency as well. From the SEM cross-section view (Fig. 1c) of the PD, it can be observed that the thicknesses of $Cs_2AgBiBr_6$ and CuSCN films are approximately to be 250 and 80 nm respectively, which basically meets the requirements of light absorption and carrier transport for the device. Fig. 1d–f depict the surface morphology of TiO_2, $Cs_2AgBiBr_6$ and CuSCN films, respectively. Particularly, for the $Cs_2AgBiBr_6$ double perovskite films, the overall grain size is large with an average size of 320 nm and pin holes are seldomly observed. With regard to the CuSCN layer, a continuous and compact film is obtained, which is beneficial to carrier transport.

To identify the composition of the CuSCN films, XPS measurement was performed. According to the survey spectrum shown in Fig. 2a, all of the expected elements (copper, sulfur, carbon and nitrogen) are detected. Additionally, the element of oxygen is present as well, which may be caused by the exposure to air. High-resolution spectra of the characteristic elements are shown in Fig. 2b–e. The Cu 2p spectrum depicts one peak at 932.7 eV, which could be assigned to Cu^+, in accordance with the previously reported literatures [30]. For the C 1s spectrum, it is fitted into two peaks. The peak at 284.6 eV is ascribed to the adventitious carbon adsorbing on the surface while the other peak at 286.2 eV is assigned to the carbon in thiocyanate functional group (–SCN) with C≡N form [31]. The spectrum of S 2p is fitted into S $2p_{1/2}$ and S $2p_{3/2}$ spin-orbit splitting with peaks at 165.0 and 163.7 eV, respectively, corresponding to the S atom in the –SCN species [31,32]. Similarly, the N 1s peak located at 398.8 eV is consistent with the C≡N bonding in the –SCN species [31,32]. The XRD pattern of the CuSCN film prepared on conventional glass substrate is presented in Fig. S5. Two distinct peaks at 16.02° and 27.06° could be assigned to the typical diffractions of (003) and (101) planes, indicating the formation of rhombohedral β-CuSCN thin film (JCPDS No.29-0581) [21]. The relatively weak peak intensity may be attributed to the thin thickness of CuSCN film.

To investigate the effects of CuSCN HTLs on the photoelectric performance and the mechanism, a PD with a structure of FTO/TiO_2/$Cs_2AgBiBr_6$ (i.e., without CuSCN layers) was prepared and used as the reference sample. Fig. S6 depicts the current-voltage (*I*-*V*) curves of

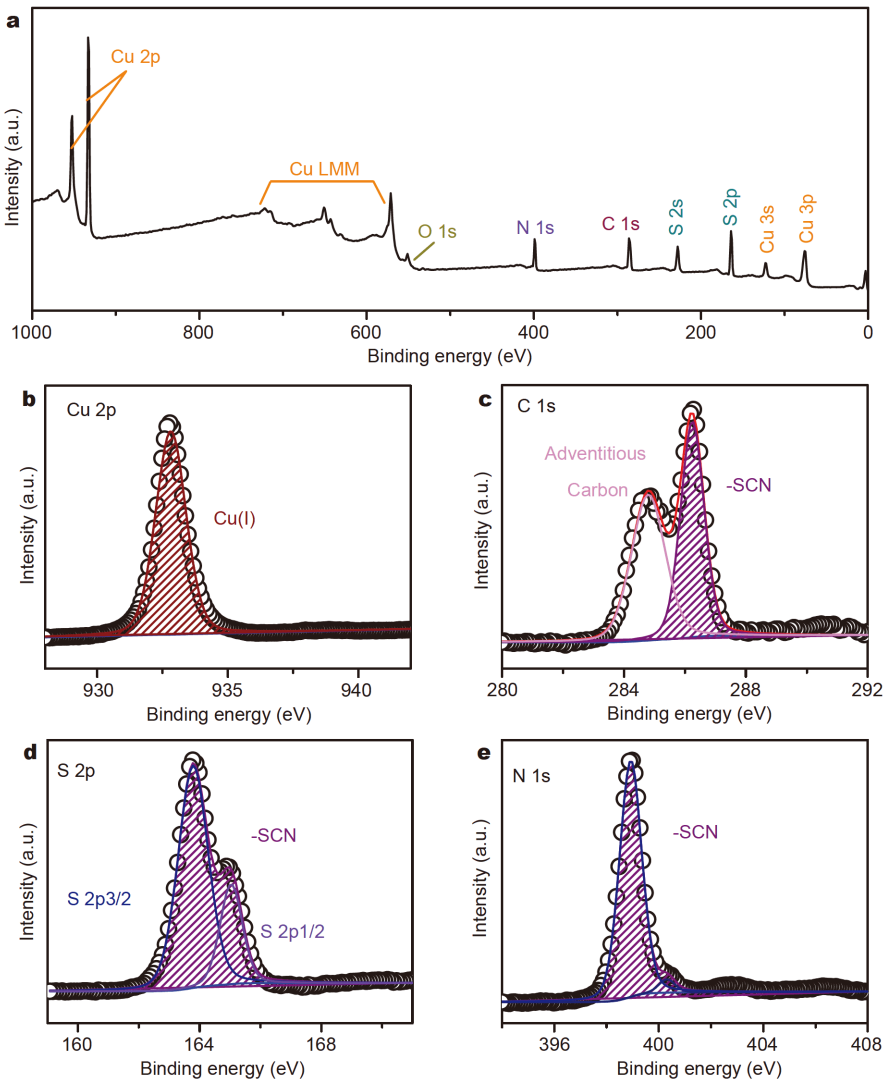

Figure 2 Component analysis of CuSCN film. (a) XPS survey spectrum of CuSCN film. High-resolution XPS spectra of (b) Cu 2p, (c) C 1s, (d) S 2p and (e) N 1s of CuSCN film. LMM: the Auger spectrum of Cu, which represents the Auger electron formed by the excitation of electron in L shell accompanying with that the vacancy is filled with electron from M shell while the released energy makes the excitation of another electron in M shell.

the samples under illumination of 0.45 mW cm^{-2} (405 nm). It is observed that both of the devices perform favorable photovoltaic characteristics, which can serve as self-powered PDs. Particularly, the *I-V* characteristic of the sample with CuSCN layer measured under dark and stronger illumination (1.5 W cm^{-2}) is presented in Fig. S7, distinctly indicating the self-powered characteristic. The typical time-dependent curves of the devices with 405-nm laser under illumination of 0.45 mW cm^{-2} at zero bias are shown in Fig. 3a for visualized comparison. Clearly, the photoresponse performance of the device with CuSCN HTL is remarkably improved, for which the on-off ratio is boosted almost an order of magnitude. The statistic box diagrams of I_{light} and I_{dark} are shown in Fig. 3c, d, respectively. Satisfyingly, with the addition of CuSCN HTL, the average I_{light} of the device increases from 7×10^{-8} to 7×10^{-7} A, soaring around tenfold compared with the reference sample. Besides, the I_{dark} almost remains equable with the value of 9×10^{-10} A. Moreover, the responsivity (R), which is an important parameter for evaluating the photodetecting efficiency, was used to assess the spectral photoresponse capability of the devices. As shown in Fig. 3b, the reference device exhibits a photoresponse ranging from 320 to 500 nm with two peaks at 370 and 440 nm, respectively. It is gratifying that the R of the device with CuSCN HTL is dramatically improved in the

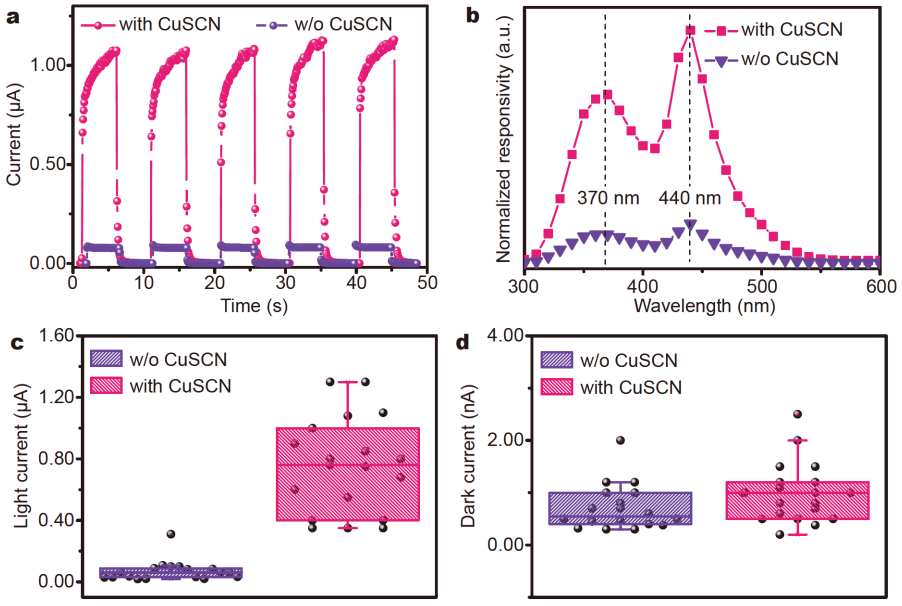

Figure 3 (a) Time-dependent photoresponse curves of the devices with and without CuSCN HTL. (b) Spectral response performances of the devices. The statistical box-plots of the corresponding (c) I_{light} and (d) I_{dark}.

whole range which could be attributed to the enhanced carrier separation capacity. In addition, the spectral photoresponse range of the device is slightly widened instead of narrowed, due to the more efficient carrier separation by the enhanced built-in potential which can be evidently found in Fig. S6.

In Fig. 4, the enhancement of photoresponse performance can be further understood from the illustrated energy-band diagram. Under light illumination, the photon-generated carriers would mainly generate in the $Cs_2AgBiBr_6$ active layer and be separated by built-in potential. For carrier transportation in ideal conditions, electrons would flow to the FTO side while the holes would go toward the Au electrode side due to the energy difference, leading to the minimized carrier recombination and the effective output of the electrical signal. However, for the reference device (Fig. 4a), compared with the $Cs_2AgBiBr_6$ film, the work function of the Au electrode is lower than its bottom of conduction-band and higher than its top of valence-band. Therefore, both electrons and holes would flow to the Au electrode side, resulting in the negative effect on the current output of the device. By utilizing a CuSCN HTL at the $Cs_2AgBiBr_6$/Au interface (Fig. 4b), it could act as a barrier for electron movement while efficiently extract the holes benefiting from the advantageous band alignment. Hence, the photodetecting efficiency of the device with TiO_2/$Cs_2AgBiBr_6$/CuSCN structure would be significantly improved. The steady-state PL spectrum was used for further evidence. As shown in Fig. S8, the $Cs_2AgBiBr_6$ film

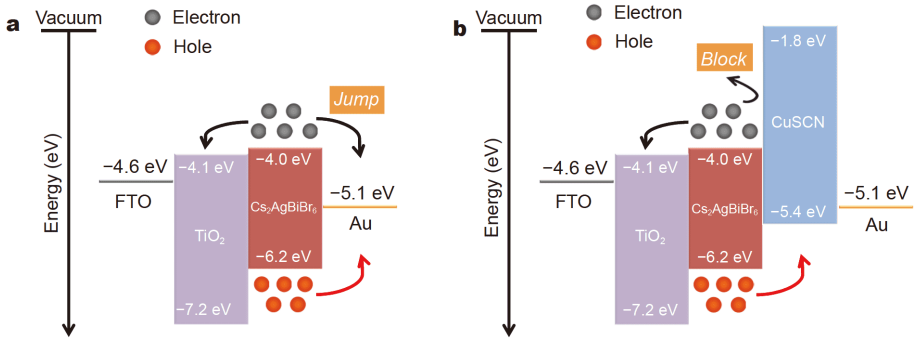

Figure 4 Energy-band analysis. Energy-band diagrams of the devices (a) with and (b) without CuSCN HTL.

exhibits a broad and distinct PL emission centered at around 620 nm. Nonetheless, in the presence of CuSCN HTL, the peak is dramatically quenched, resulting from the optimized band alignment with rapid extraction of carriers across the interface [27].

Concerning on the weak light response performance of the devices, the weak light detection limit of the reference sample is estimated to be ~7×10^{-9} W cm^{-2} since it is the minimum intensity of light for the device to remain distinct and regular rectangle photoresponse curves (Fig. 5a). Meanwhile, the D^*, another essential factor which represents the capability of a PD for weak optical signal detections, is calculated to be 1.74×10^{12} Jones following the equation of $D^*=[(I_{light}-I_{dark})/I_{light}]/(2qI_{dark})^{1/2}$, where q is the elementary charge [33]. In addition, a responsivity of 0.04 A W^{-1} was obtained. With regard to the device with CuSCN HTL, it is encouraging that the weak light detection limit remarkably reduces to as low as ~1×10^{-9} W cm^{-2} (Fig. 5b), which could be attributed to the enhanced carrier separation efficiency. In consequence, the R and D^* are up to 0.34 A W^{-1} and 1.03×10^{13} Jones, respectively. Table 1 lists performance comparison of previous reported $Cs_2AgBiBr_6$-based PDs. It is pleasant that the device with CuSCN HTL shows superior I_{dark} and D^*. Moreover, the linear dynamic range (LDR) of the devices was also calculated using the following expression: LDR (dB) = $20\log(P_{max}/P_{min})$, where P_{max} and P_{min} are the highest and lowest incident light powers of the range, respectively, in which the PD response is linear with the incident power [33]. As shown in Fig. 5c, d, benefiting from the enhanced weak light photoresponse performance, the LDR of the PD with CuSCN HTL is extended from 99.8 to 126.8 dB, which is superior to the commercially available Si (120 dB) and InGaAs (66 dB) PDs [35]. The comparison of photocurrent as a function of incident power is shown in Fig. S9. It is found that the photocurrent increase of the device with CuSCN becomes more obvious with lower illumination, suggesting the promising potential for weak light imaging. Fig. S10 presents the enlarged photoresponse curves of rise/decay edges for the devices which were obtained under a frequency of 10 Hz. The rise/decay times of the PD with CuSCN HTL slightly decline from 20.09/26.48 to 28.75/32.95 ms. Furthermore, the stability results of the devices are shown in Fig. S11. It should be noted that the $Cs_2AgBiBr_6$ thin film demonstrates satisfying stability in ambient air. Nevertheless, it is still unstable in high-humidity environment due to the perovskite feature itself. In this case, we designedly store both devices in constant high-humidity cabinet (50% relative humidity (RH)) on the purpose to reveal the effect of CuSCN layer on humidity stability. We measured

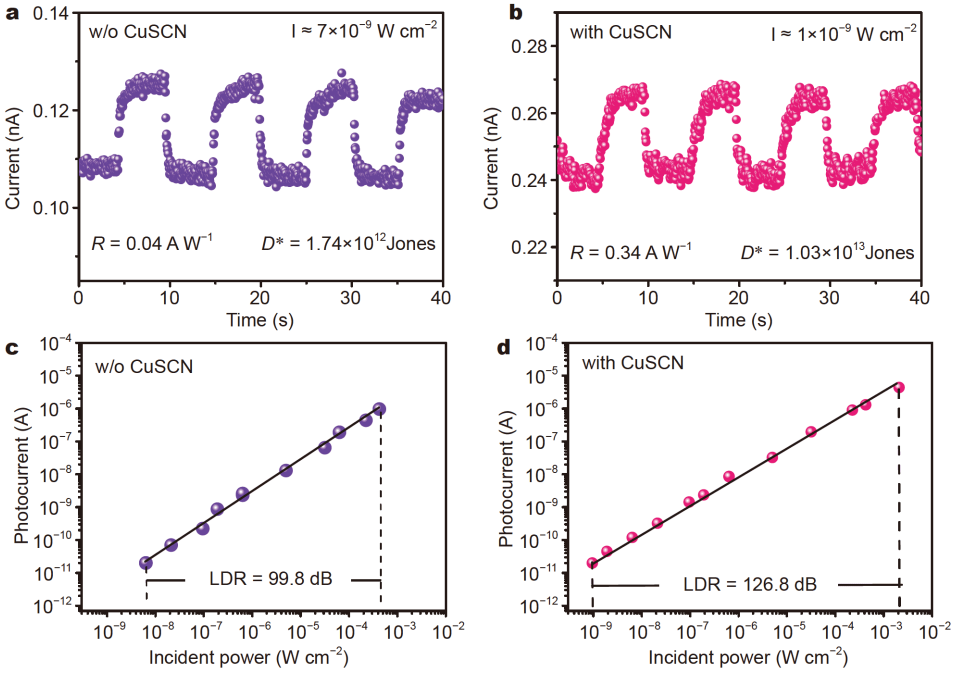

Figure 5 Performance comparison. The photoresponse curves of the devices (a) without and (b) with CuSCN HTL under weak light detection limit illumination. The corresponding LDRs of the devices (c) with and (d) without CuSCN HTL.

Table 1 Comparison of photoresponse performances of $Cs_2AgBiBr_6$-based PDs reported in previous literatures

Device structure	Measurement condition	I_{dark} (A)	R (A W^{-1})	D^* (Jones)	Ref.
Au/$Cs_2AgBiBr_6$/Au	5 V, 404 nm	N/A[a]	7.01	5.66×10^{11}	[19]
ITO[b]/SnO_2/$Cs_2AgBiBr_6$/Au	0 V, 435 nm	9.5×10^{-9}	0.11	2.4×10^{10}	[34]
ITO/SnO_2/$Cs_2AgBiBr_6$/TFB/Au	0 V, 445 nm	N/A	0.14	3.3×10^{12}	[35]
In/GaN-$Cs_2AgBiBr_6$/Ag	0 V, 5 μW cm^{-2}	N/A	1.46	0.94×10^{13}	[36]
FTO/TiO_2/$Cs_2AgBiBr_6$/CuSCN/Au	0 V, 405 nm, ~1 nW cm^{-2}	2.4×10^{-10}	0.34	1.03×10^{13}	This work

a) N/A=not applicable; b) ITO is indium tin oxide.

the current-time (*I-t*) curves of the samples after storing them for 30 and 60 d and compared them with the initial ones. It is found that the PD with CuSCN HTL shows favorable stability after being stored for 60 d and ~83% of the photocurrent retains while the photocurrent of the reference device drops to ~40% under the same condition. It is known that CuSCN film is a kind of inorganic material, which would not react with the perovskite materials, unlike the organic compound [27]. In this case, the upper CuSCN HTL would act as a protective layer, reducing the influence of moisture on the $Cs_2AgBiBr_6$ films and the device performance and consequently improving the stability. Moreover, the results also indicate that the quality of $Cs_2AgBiBr_6$ thin film is the main factor affecting the stability of the corresponding device, rather than CuSCN HTL.

Additionally, both of the PDs were integrated into a self-built light detection imaging system and served as imaging sensors for weak light imaging. The imaging system utilizes the focused laser scanning imaging mode, adopting a transmission imaging method. The schematic of the system is shown in Fig. 6a. In brief, once the laser shines on and scans the patterns point-to-point, the PD detects the transmitted light and outputs the related electric signals for the computer to work out the images by specific algorithms. Fig. 6b, c reveal the imaging results provided by the two different PDs under the illumination of 50 nW cm^{-2}. Fig. 6d depicts the corresponding *I-t* curves of the PDs. The size of the pattern is 5 cm×5 cm. It is evident that using the PD with CuSCN HTL can obtain much better imaging results. In Fig. 6b, the image produced by the reference PD becomes quite fuzzy under such illumination condition, especially the words in the pattern. The signal-to-noise ratio (SNR), defined as the ratio of the mean output current to the standard deviation of the output current [37,38], shows inhomogeneity in the whole image as well, resulting from the unstable outputs during the imaging process. As shown in Fig. 6e, the current drift of the reference PD is observed in the amplified *I-t* curve, which would prominently affect the point-to-point imaging under circumstance of low SNR. As for the current drift, it could be attributed to the tiny external disturbance during the imaging process, which becomes apparent in the case of very low output current. Nevertheless, its influence would be weakened once the photocurrent is increased. On the contrary, the image given by the PD with CuSCN HTL can still be well recognized under the same illumination condition whether graphics or words (Fig. 6c). To further explore the weak light detection and imaging capability of the PD with CuSCN HTL, Fig. 6g–i exhibit the imaging results under the illumination ranging from 200 to 5 nW cm^{-2}, compared with the initial pattern (Fig. 6f). With 200 nW cm^{-2} illumination, the imaging is almost identical to the pattern, including the brightness and contrast. When the illumination is lowered to 100 nW cm^{-2}, the imaging remains clear though the SNR gets lower. Encouragingly, the imaging produced with illumination of as low as 5 nW cm^{-2} can still reveal the details of the pattern, demonstrating the promising potential of the $Cs_2AgBiBr_6$-based PHJ PDs for weak light imaging applications.

CONCLUSIONS

In summary, all-inorganic PHJ self-powered PDs with TiO_2/$Cs_2AgBiBr_6$/CuSCN structure were fabricated for the first time. Benefiting from the favorable optical property of CuSCN films, the AVT of the device reached 62.82%, demonstrating the promising potential for semi-transparent devices. The effects of CuSCN HTLs on the photoresponse performance were investigated in detail. In the presence of CuSCN HTL, both the I_{light} and on-off ratio of the PD significantly increased by almost an order of magnitude. In addition, for spectral photoresponse performance, the responsivity was remarkably improved in the whole range. It is revealed that the positive effect of CuSCN HTL on the photoresponse performance is attributed to the optimized band alignment, leading to the efficient transport of holes and the blocking of electrons at the $Cs_2AgBiBr_6$/CuSCN interface. With regard to the weak light response performance, the weak light detection

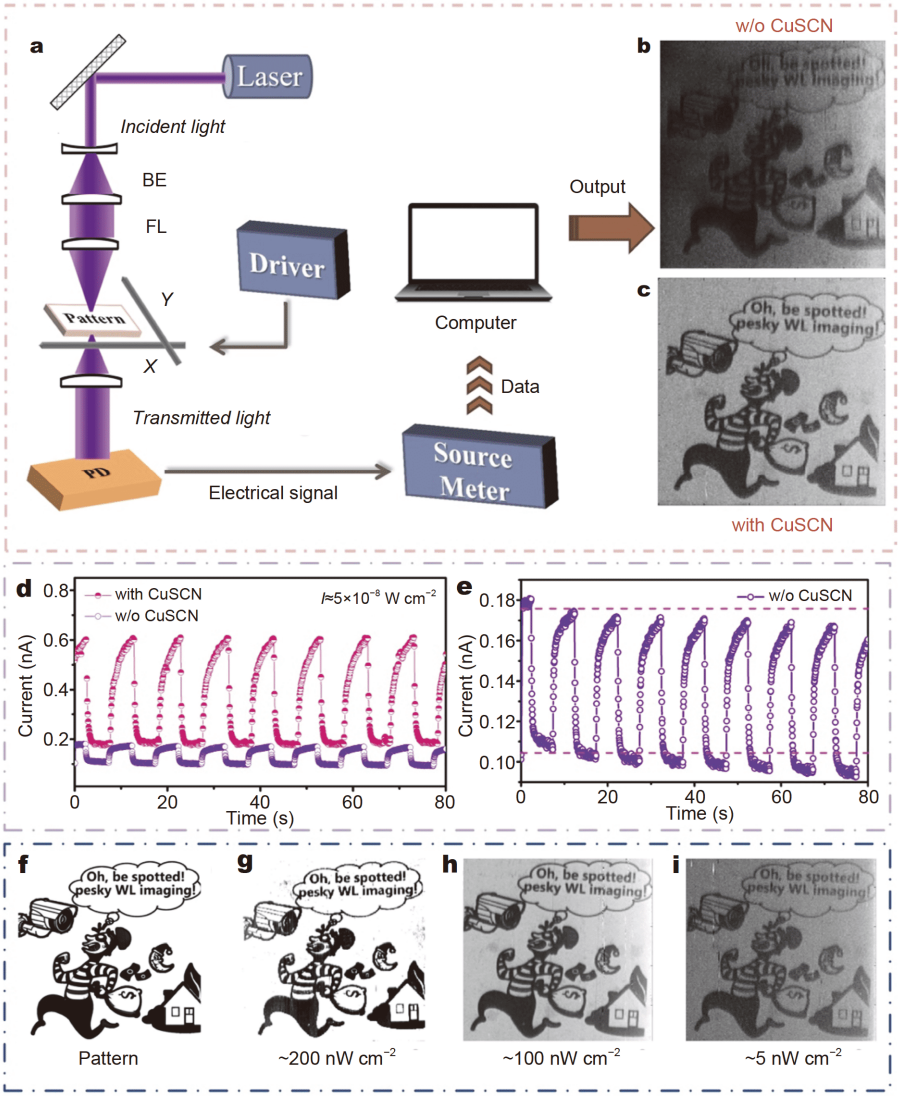

Figure 6 Imaging performances. (a) Schematic of the self-built light detection imaging system. Imaging results of the PDs (b) without and (c) with CuSCN layer under 50 nW cm^{-2} illumination. (d) *I-t* curves of the PDs under illumination of 50 nW cm^{-2}. (e) Amplified *I-t* curve of the reference PD. Imaging comparison of (f) the pattern and the imaging results with illuminations of (g) 200 nW cm^{-2}, (h) 100 nW cm^{-2} and (i) 5 nW cm^{-2}. FL: focus lens; BE: beam expander.

limit of the PD with CuSCN HTL prominently decreased from ~7×10^{-9} to ~1×10^{-9} W cm^{-2}, resulting in the extension of LDR to 126.8 dB. Moreover, the corresponding R and D^* rose up to 0.34 A W^{-1} and 1.03×10^{13} Jones, respectively, which are superior to the reported $Cs_2AgBiBr_6$-based PDs. Furthermore, the PDs were integrated into a self-built light detection imaging system for weak light imaging. For the image provided by the PD with CuSCN HTL, the related graphics and words can still be well recognized with an illumination of as low as 5 nW cm^{-2}, while the reference PD has already provided fuzzy image with an illumination of 50 nW cm^{-2}. These results indicate the great potential of the all-inorganic $TiO_2/Cs_2AgBiBr_6$/CuSCN PHJ PDs for weak light imaging applications.

Received 24 February 2020; accepted 15 April 2020; published online 3 July 2020

1 Wang L, Jie J, Shao Z, *et al.* MoS_2/Si heterojunction with vertically standing layered structure for ultrafast, high-detectivity, self-driven visible-near infrared photodetectors. Adv Funct Mater, 2015, 25: 2910–2919
2 Leung SF, Ho KT, Kung PK, *et al.* A self-powered and flexible organometallic halide perovskite photodetector with very high detectivity. Adv Mater, 2018, 30: 1704611

3 Zhang Y, Du J, Wu X, *et al.* Ultrasensitive photodetectors based on island-structured $CH_3NH_3PbI_3$ thin films. ACS Appl Mater Interfaces, 2015, 7: 21634–21638
4 Wang A, Fu L, Zhang Y,et al. High-sensitivity photon-counting imaging detector. In: Proceedings of SPIE. Beijing, 2004. 439–442
5 Ding L, Li YQ, Liu XY, *et al.* Weak light characteristics of potential biosensor unit. Micro-Nano Lett, 2013, 8: 594–597
6 Dong Q, Fang Y, Shao Y, *et al.* Electron-hole diffusion lengths >175 μm in solution-grown $CH_3NH_3PbI_3$ single crystals. Science, 2015, 347: 967–970
7 Stranks SD, Eperon GE, Grancini G, *et al.* Electron-hole diffusion lengths exceeding 1 micrometer in an organometal trihalide perovskite absorber. Science, 2013, 342: 341–344
8 Yang WS, Park BW, Jung EH, *et al.* Iodide management in formamidinium-lead-halide-based perovskite layers for efficient solar cells. Science, 2017, 356: 1376–1379
9 Jeon NJ, Na H, Jung EH, *et al.* A fluorene-terminated hole-transporting material for highly efficient and stable perovskite solar cells. Nat Energy, 2018, 3: 682–689
10 Cho H, Jeong SH, Park MH, *et al.* Overcoming the electroluminescence efficiency limitations of perovskite light-emitting diodes. Science, 2015, 350: 1222–1225
11 Lin K, Xing J, Quan LN, *et al.* Perovskite light-emitting diodes with external quantum efficiency exceeding 20 percent. Nature, 2018, 562: 245–248
12 Yang T, Zheng Y, Du Z, *et al.* Superior photodetectors based on all-inorganic perovskite $CsPbI_3$ nanorods with ultrafast response and high stability. ACS Nano, 2018, 12: 1611–1617
13 Saidaminov MI, Adinolfi V, Comin R, *et al.* Planar-integrated single-crystalline perovskite photodetectors. Nat Commun, 2015, 6: 8724
14 Tan Z, Wu Y, Hong H, *et al.* Two-dimensional $(C_4H_9NH_3)_2PbBr_4$ perovskite crystals for high-performance photodetector. J Am Chem Soc, 2016, 138: 16612–16615
15 Ji C, Wang P, Wu Z, *et al.* Inch-size single crystal of a lead-free organic-inorganic hybrid perovskite for high-performance photodetector. Adv Funct Mater, 2018, 28: 1705467
16 Tong XW, Kong WY, Wang YY, *et al.* High-performance red-light photodetector based on lead-free bismuth halide perovskite film. ACS Appl Mater Interfaces, 2017, 9: 18977–18985
17 Zhou J, Luo J, Rong X, *et al.* Lead-free perovskite derivative $Cs_2SnCl_{6-x}Br_x$ single crystals for narrowband photodetectors. Adv Opt Mater, 2019, 7: 1900139
18 Luo J, Li S, Wu H, *et al.* $Cs_2AgInCl_6$ double perovskite single crystals: Parity forbidden transitions and their application for sensitive and fast UV photodetectors. ACS Photonics, 2017, 5: 398–405
19 Lei LZ, Shi ZF, Li Y, *et al.* High-efficiency and air-stable photodetectors based on lead-free double perovskite $Cs_2AgBiBr_6$ thin films. J Mater Chem C, 2018, 6: 7982–7988
20 Wang A, Yan X, Zhang M, *et al.* Controlled synthesis of lead-free and stable perovskite derivative Cs_2SnI_6 nanocrystals *via* a facile hot-injection process. Chem Mater, 2016, 28: 8132–8140
21 Jung JW, Chueh CC, Jen AKY. High-performance semitransparent perovskite solar cells with 10% power conversion efficiency and 25% average visible transmittance based on transparent CuSCN as the hole-transporting material. Adv Energy Mater, 2015, 5: 1500486
22 Liu D, Kelly TL. Perovskite solar cells with a planar heterojunction structure prepared using room-temperature solution processing techniques. Nat Photon, 2013, 8: 133–138
23 Cao J, Wu B, Chen R, *et al.* Efficient, hysteresis-free, and stable perovskite solar cells with ZnO as electron-transport layer: effect of surface passivation. Adv Mater, 2018, 30: 1705596
24 Jiang Q, Zhang L, Wang H, *et al.* Enhanced electron extraction using SnO_2 for high-efficiency planar-structure $HC(NH_2)_2PbI_3$-based perovskite solar cells. Nat Energy, 2016, 2: 16177
25 Zhou H, Chen Q, Li G, *et al.* Interface engineering of highly efficient perovskite solar cells. Science, 2014, 345: 542–546
26 Zhang P, Yu Q, Min X, *et al.* Fabrication of $Cu_2ZnSn(S,Se)_4$ photovoltaic devices with 10% efficiency by optimizing the annealing temperature of precursor films. RSC Adv, 2018, 8: 4119–4124
27 Arora N, Dar MI, Hinderhofer A, *et al.* Perovskite solar cells with CuSCN hole extraction layers yield stabilized efficiencies greater than 20%. Science, 2017, 358: 768–771
28 Qin P, Tanaka S, Ito S, *et al.* Inorganic hole conductor-based lead halide perovskite solar cells with 12.4% conversion efficiency. Nat Commun, 2014, 5: 3834
29 Wijeyasinghe N, Regoutz A, Eisner F, *et al.* Copper(I) thiocyanate (CuSCN) hole-transport layers processed from aqueous precursor solutions and their application in thin-film transistors and highly efficient organic and organometal halide perovskite solar cells. Adv Funct Mater, 2017, 27: 1701818
30 Zhao Z, Yang H, Zhu Y, *et al.* Interfacial N–Cu–S coordination mode of $CuSCN/C_3N_4$ with enhanced electrocatalytic activity for hydrogen evolution. Nanoscale, 2019, 11: 12938–12945
31 Jaffe JE, Kaspar TC, Droubay TC, *et al.* Electronic and defect structures of CuSCN. J Phys Chem C, 2010, 114: 9111–9117
32 Aldakov D, Chappaz-Gillot C, Salazar R, *et al.* Properties of electrodeposited CuSCN 2D Layers and nanowires influenced by their mixed domain structure. J Phys Chem C, 2014, 118: 16095–16103
33 Liang Z, Zeng P, Liu P, *et al.* Interface engineering to boost photoresponse performance of self-powered, broad-bandwidth PEDOT:PSS/Si heterojunction photodetector. ACS Appl Mater Interfaces, 2016, 8: 19158–19167
34 Wu C, Du B, Luo W, *et al.* Highly efficient and stable self-powered ultraviolet and deep-blue photodetector based on $Cs_2AgBiBr_6/SnO_2$ heterojunction. Adv Opt Mater, 2018, 6: 1800811
35 Yang J, Bao C, Ning W, *et al.* Stable, high-sensitivity and fast-response photodetectors based on lead-free $Cs_2AgBiBr_6$ double perovskite films. Adv Opt Mater, 2019, 7: 1801732
36 Li Y, Shi Z, Lei L, *et al.* Ultrastable lead-free double perovskite photodetectors with imaging capability. Adv Mater Interfaces, 2019, 6: 1900188
37 Zhou X, Hobbs MJ, White BS, *et al.* An InGaAlAs-InGaAs two-color photodetector for ratio thermometry. IEEE Trans Electron Devices, 2014, 61: 838–843
38 Kulkarni M, Gruev V. Integrated spectral-polarization imaging sensor with aluminum nanowire polarization filters. Opt Express, 2012, 20: 22997–23012

Acknowledgements This work was supported by the National Natural Science Foundation of China (51772135), the Ministry of Education of China (6141A02022516), the Fundamental Research Funds for the Central Universities (11619103), China Postdoctoral Science Foundation (2019M663376), Guangdong Province Higher Vocational Colleges & Schools Pearl River Scholar Funded Scheme (2017), the Natural Science Foundation of Guangdong Province, China (2017A020215135 and 2018A030310659) and the Science and Technology Program of

Guangzhou, China (201804010432).

Author contributions Yan G designed and engineered the device samples and wrote the paper; Ji Z designed and engineered the imaging system; Li Z and Jiang B performed the chemical experiments; Yan G, Kuang M and Cai X accomplished the characterizations; Yuan Y proposed the idea and analyzed the data. This work was guided and supported by Mai W. All authors contributed to the general discussion.

Conflict of interest The authors declare that they have no conflict of interest.

Supplemetary information Supporting data are available in the online version of the paper.

Genghua Yan received her BSc degree in applied physics from Central South University in 2013 and PhD degree in materials physics and chemistry from Sun Yat-Sen University (SYSU) in 2018. She joined the College of Science and Engineering, Jinan University as a postdoctor since the middle of 2018. Her main research interest focuses on advanced thin film materials and photoelectric devices.

Ye Yuan received his BSc degree in optical information science and technology from SYSU in 2013 and PhD degree in materials physics and chemistry from SYSU in 2018. He now is an assistant research fellow at the Department of Physics, Jinan University. His research interests are thin-film photoelectric materials and devices, especially heterojunction photodetectors and solar cells.

Wenjie Mai is a professor as well as head of the Deparment of Physics, Jinan University. He received his BSc degree from Peking University in 2002 and PhD degree from Georgia Institute of Technology (GIT) in 2009. He joined Jinan University in 2009. He was a visiting fellow at GIT from 2012 to 2013. His research areas include photoelectric materials, energy materials and the related flexible devices. He currently focuses on supercapacitors, photodetectors and solar cells.

全无机$Cs_2AgBiBr_6$/CuSCN基光电探测器及其在弱光成像中的应用

颜庚骅[1], 计钟[1], 李卓伟[1], 江邦齐[1], 况敏[3], 蔡祥[4], 袁野[1*], 麦文杰[1,2*]

摘要 弱光成像技术在安全监测、空间勘探、医疗成像及通讯领域有着广泛的应用. 光电探测器是弱光成像技术的核心元件, 决定了成像系统的质量. 本工作首次将硫氰酸亚铜(CuSCN)薄膜作为无机空穴传输层(HTLs)与全无机$Cs_2AgBiBr_6$双钙钛矿薄膜相结合, 获得了具有优良弱光探测能力的光电探测器. CuSCN薄膜具有优异的空穴提取能力, 可以有效地传输空穴并调节能带排列, 从而减少载流子在$Cs_2AgBiBr_6$/CuSCN界面处的复合, 使器件的光电流提升近10倍. 该器件在~1 nW cm^{-2}的弱光下的响应度和探测率分别达到了0.34 A W^{-1}和1.03×10^{13} Jones. CuSCN薄膜还具有优异的光透过率, 保证了器件的半透明特性. 我们搭建了基于聚焦激光扫描成像模式的弱光成像系统, 并将$Cs_2AgBiBr_6$/CuSCN异质结光电探测器集成于该系统中. 采用一幅包含图形和文字的图案(尺寸为5 cm×5 cm)为成像对象. 在低至5 nW cm^{-2}(405 nm)的辐照下, 该系统依然能够输出清晰的图像. 这些研究结果显示了基于$Cs_2AgBiBr_6$/CuSCN结构的全无机光电探测器在弱光探测和成像领域的巨大潜力.

